OCEANOGRAPHY

Dominant frazil ice production in the Cape Darnley polynya leading to Antarctic Bottom Water formation

Kay I. Ohshima[1,2]*, Yasushi Fukamachi[2], Masato Ito[3], Kazuki Nakata[4], Daisuke Simizu[3], Kazuya Ono[1], Daiki Nomura[2,5], Gen Hashida[3], Takeshi Tamura[3]

Antarctic Bottom Water (AABW) occupies the abyssal layer of the world ocean and contributes to the global overturning circulation. It originates from dense shelf water, which forms from brine rejection during sea ice production. An important region of AABW formation has been identified off the Cape Darnley polynya. However, it remains unclear why and how high ice production leads to AABW formation. Using moored acoustic measurements and a satellite microwave algorithm, we reveal that underwater frazil ice dominates in the polynya. This underwater ice formation prevents heat-insulating surface-cover ice forming, thereby enabling efficient ice production. The high ice production in the nearshore and longer residence times create high-salinity source water for the AABW. Underwater frazil ice occurs as long as strong winds continue and occasionally penetrates depths of at least 80 m. Deep-penetrating frazil ice is particularly prominent in this polynya, while it also occurs in other Antarctic coastal polynyas.

INTRODUCTION

Antarctic Bottom Water (AABW) forms at the Antarctic margin and feeds the abyssal layer (1), accounting for 30 to 40% of the global ocean mass (2). AABW production contributes to global overturning circulation and serves as an important heat sink (3). Dense shelf water (DSW), which forms on the continental shelf by brine rejection from sea ice production and ocean/ice-shelf interactions, descends down the shelf slope and mixes with the overlying modified Circumpolar Deep Water (mCDW) to form AABW. The Weddell and Ross seas, with major continental ice shelves, are two distinct sites of AABW formation. The third region of the AABW formation was identified off the Adélie Coast (4), where enhanced sea ice production in the coastal polynya directly causes DSW/AABW formation (5).

Motivated by the satellite estimate of high sea ice production at the Cape Darnley polynya (CDP) west of the Amery Ice Shelf (Fig. 1) (6), mooring measurements were conducted in the canyon off this polynya, revealing that AABW is formed there (7). This fourth type of AABW (8) is referred to as Cape Darnley Bottom Water (CDBW) (7). CDBW is advected westward to contribute to the Weddell Sea Deep Water (9–11). The discovery of CDBW has been followed by a series of studies. The ventilation by CDBW was confirmed by several studies (11–13). The role of turbulent mixing (14) and carbonate chemistry (15) in the DSW overflow in this region were examined on the basis of summer ship-based observations. Pathways and time scales of the spread of CDBW was quantified using transient tracers (16). Further, historical and repeat hydrographic observations revealed multidecadal changes in CDBW: freshening on the continental slope and warming in the deep basin (10, 17, 18). Regional numerical models reproduced the formation and variability of CDBW (19, 20). High-resolution global models well represented CDBW in addition to three other AABW sources (21, 22).

Unlike the area off the Adélie Coast with a large depression being a reservoir of DSW, the CDP area does not have such a large depression of the reservoir and thus requires particularly high ice production to create high-salinity dense water as the AABW source. However, observations have been limited to offshore areas, and it remains unclear why and how the dense source water is formed in the CDP.

Under cold and windy conditions, sea ice is initially generated as fine disk-shaped or dendritic crystals, called frazil ice (23), which remain disaggregated when turbulent mixing is vigorous. Recently, underwater frazil ice formation as deep as ~50 m was indirectly suggested by the temperature and salinity profiles in the Terra Nova Bay polynya (24). It has also been shown that supercooling occurs widely throughout the Antarctic coastal waters (25), in addition to that originating from ice-shelf/seawater interactions. The newly developed algorithm of Advanced Microwave Scanning Radiometer (AMSR) for ice-type classification (26) suggested that active frazil, a mixture of frazil/pancake ice streaks and open water, predominates at both the CDP and Terra Nova Bay polynya (27). If active frazil dominates, then large heat loss and therefore high ice production are expected because of decreased heat insulation due to reduced surface ice cover.

We conducted mooring observations with acoustic Doppler current profilers (ADCPs) and conductivity-temperature (CT) recorders inside the CDP throughout winter. To examine the relationship between water mass formation and ice production, we analyzed both water properties and sea ice using moored acoustic measurements and our satellite microwave (AMSR) algorithm, which detects active-frazil areas.

RESULTS

The dominance of underwater frazil ice

Two moorings were deployed near the shore (a1) and the shelf edge (a2) (Fig. 1A). The details of the moorings are summarized in table S1. From the ADCP, the volume backscatter strength (SV) could be derived (see Materials and Methods). At a2, two CT recorders were attached, one at 86-m depth, referred to as the upper layer, and the other at 226-m depth, referred to as the lower layer. In Fig. 1, we map the annual sea ice production and the occurrence rate of the active-frazil area, estimated using the AMSR algorithm of thin ice
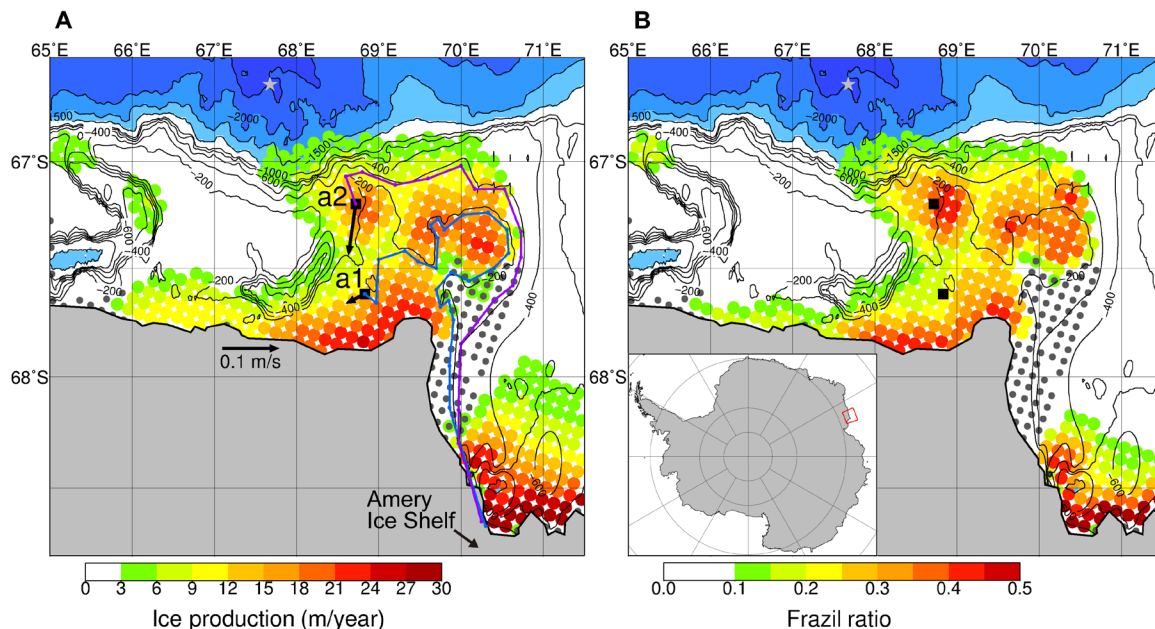
Fig. 1. Map of sea ice production and active-frazil area in the CDP. (**A**) Annual sea ice production and (**B**) occurrence rate of active frazil during the freezing period (February–November) of 2010. Areas of landfast sea ice with an occurrence rate of >50% detected by the algorithm (*36*) are shown by gray dots. The bathymetry obtained from the general bathymetric chart of the oceans data is indicated by black contours with 200-m intervals for <1000 m and 500-m intervals for >1000 m (blue shadings). In (A), mooring locations are indicated by squares with the mean velocity at a depth of 57 m (a1) and 67 m (a2). The gray star indicates the mooring location where the CDBW outflow was observed along the canyon (*7*). The inset in (B) shows the location of the study area (red rectangle).

thickness with ice-type classification (*26*) and a heat flux calculation (see Materials and Methods). The monthly ice production maps are shown in fig. S1. The year of the mooring observation (2010) shows an annual ice production of 164 km^3, which is only 12% lower than the average, and thus represents a relatively typical year of sea ice production (figs. S2 and S3).

Figure 2 summarizes the time series of the mooring data with the atmospheric conditions and the AMSR sea ice products during the freezing season. In the vertical profile of the SV (Fig. 2, C and D), deep-penetrating acoustic signals with SV > ~−80 dB appear in tandem with strong wind events (Fig. 2A). Furthermore, these signals coincide with a high active-frazil ratio and a high ice production rate derived from the satellite (Fig. 2B). Figure 2 demonstrates that the time series of the quantities from three independent sources—atmospheric reanalysis, satellite microwave, and moored instruments—show strongly coherent variations. The SV at a1 is highly correlated with wind speed (Fig. 3A), the active-frazil ratio (Fig. 3B), and sea ice production (Fig. 3C). Similar high correlations are also identified at a2 (fig. S4). From late March through October, when high-SV events occasionally occur, a potential supercooling of ~10 mK is shown stably at a1 and sporadically at a2 underneath the ADCP (light blue shading in Fig. 2, E to G), although the reliability of supercooling should be carefully considered (see Materials and Methods).

Together, we conclude that the deeply penetrating signals are due to backscatter from the suspended frazil ice. It should also be noted that satellite microwaves measuring the ice/ocean surface could provide information on underwater frazil ice. Most unexpectedly, the ADCP SV reveals that frazil ice can penetrate 70 to 80 m (Fig. 2, C and D) or even more inferred from supercooling at the CT recorders underneath the ADCPs. The observed penetrating depths are much deeper than the 30- to 40-m depth previously reported for

several coastal polynyas using acoustic instruments (*28–31*). Our observed frazil ice likely originates from cooling from the surface and differs from the frazil (platelet) ice originating from ice-shelf/ seawater interactions (*32–35*).

Here, we examine the relationship between the penetration depth of frazil ice and wind, although it is difficult to precisely define the penetration depth. We chose two threshold values of SV, −80 and −90 dB, as indices of the high and low signals of frazil ice, respectively. Then, we find the deepest bin at which SV exceeds these two threshold values on a 6-hour basis and define the average of these two bin depths as the penetration depth. A scatter plot between the penetration depth and wind speed (Fig. 3D) suggests that the wind speed is a key determinant factor for the penetration depth of frazil ice.

According to the lag correlation of SV at a1 with wind speed, all depths show a maximum correlation at a 3-hour lag, with a sharp decrease in the correlation within a 1-day lag (Fig. 3E). From March to November, there were 35 polynya events that accompanied active underwater frazil ice, and the duration of these polynya events strongly correlates with the length of time of wind speeds exceeding 15 m s^{-1} (Fig. 3F), indicating that a frazil ice event is controlled by the wind. These results imply that underwater frazil ice occurs immediately after the onset of strong turbulence and cooling by the wind and disappears soon after the wind calms down, probably by quickly floating and transforming into consolidated thin ice at the surface. These relationships with wind are consistent with the results in the Terra Nova Bay polynya (*24*).

Such transformation is suggested by a time series of the AMSR ice-type products and synthetic aperture radar images in which active-frazil regions with high backscatter streaks transform into thin solid-ice regions with relatively uniform backscatter when the wind ceases (figs. S5 and S6). If the AMSR sea ice products are assumed
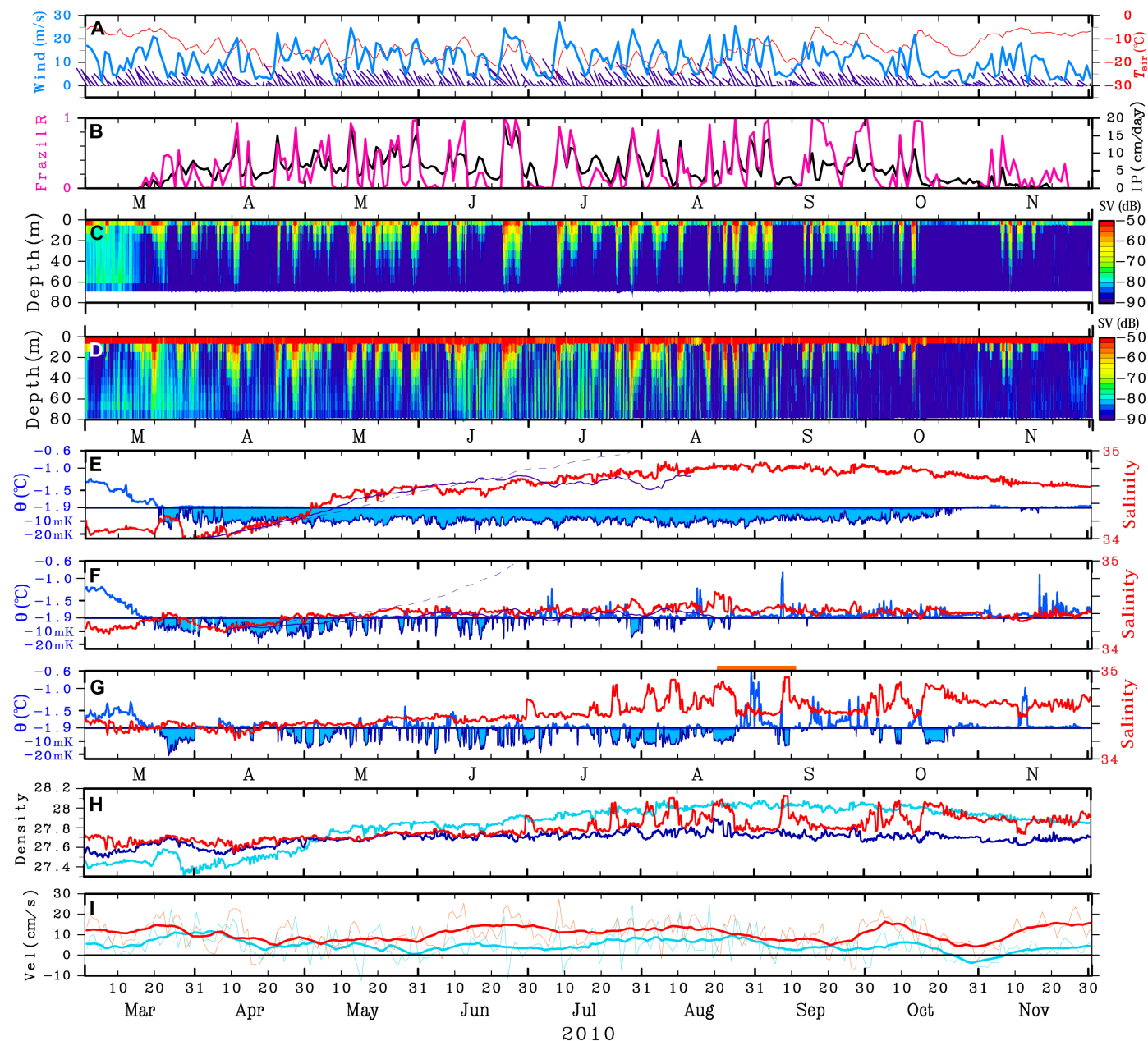
Fig. 2. Time series of mooring data, atmospheric condition, and AMSR sea ice products, from March through November 2010. (**A**) Wind vectors (purple sticks) with northward being up, wind speed (blue), and air temperature (red) near a1 from the ERA5. (**B**) Occurrence rate of frazil ice (pink) and daily sea ice production (IP) (black) at a1 derived from the AMSR-E data. (**C** and **D**) Vertical profile of the ADCP volume backscatter strength (SV) at a1 (C) and a2 (D). (**E** to **G**) Salinity (red) and potential temperatures (blue) with degree of potential supercooling (light blue shading) at 128 m at a1 (E), 86 m at a2 (F), and 226 m at a2 (G). In (E) and (F), salinity results from the backward-tracking method and local budget are superimposed by purple solid and dashed lines, respectively. In (E) to (G), temperatures below −1.9°C (approximate freezing point) are scaled in millikelvins to represent degree of supercooling. (**H**) Potential density at 128 m at a1 (light blue), 86 m at a2 (dark blue), and 226 m at a2 (red). (**I**) Velocity components in the mean flow direction at 57 m at a1 (light blue) and 67 m at a2 (red) with 15-day running means (thick lines).

to be correct, then sea ice production in active-frazil areas is nearly twice as large as that in thin solid-ice areas in the entire CDP area (fig. S3). The total ice production is also notably higher than the previous estimates (*36*, *37*), which could not discriminate frazil ice.

Salinity changes due to sea ice production
High sea ice production increases shelf water salinity through brine rejection. As expected, the salinity at nearshore site a1 increases rapidly

from April after the start of ice production (Fig. 2, B and E). However, the rate of salinity increase diminishes after June despite continued ice production. After a peak salinity of ~34.8 in September, values decrease. At shelf edge site a2, the salinity of the upper layer increases only up to ~34.5 by May and then remains relatively unchanged despite continued ice production (Fig. 2F). Briefly, the observed salinity variation at a1 and a2 cannot be explained solely by local ice production, which implies that water mass advection and diffusion also contribute.
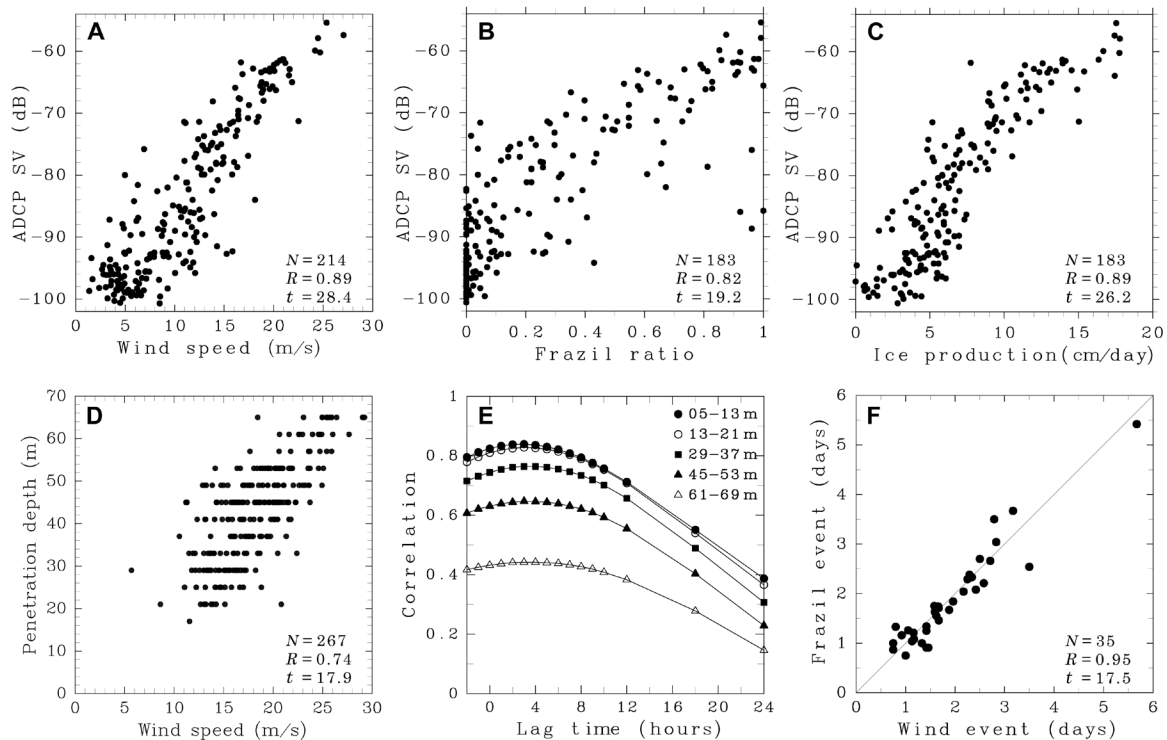
Fig. 3. Relationship among detected underwater frazil ice, wind, and AMSR sea ice products at mooring a1. (**A** to **C**) Scatter plot of ADCP SV at a bin of 5 to 13 m with (A) wind speed during April–October, (B) active-frazil ratio from the AMSR algorithm during April–September, and (C) sea ice production during April–September, on a daily basis. (**D**) Scatter plot of wind speed versus penetration depth of frazil ice on a 6-hour basis during April–October, when the SV at 5 to 13 m exceeds −75 dB, where the penetration depth of frazil ice is defined as the average of the greatest depths at which SV exceeds −80 and −90 dB. (**E**) Lag correlations of SV at bins of 5 to 13, 13 to 21, 29 to 37, 45 to 53, and 61 to 69 m with wind speed on an hourly basis. (**F**) Scatter plot of frazil event time versus wind event time during March–November, where a frazil event is defined as a case that the SV at 5 to 13 m exceeds −77 dB continuously for more than 18 hours, and a wind event time is defined as the duration that the wind speed exceeds 15 m s^{-1} for the corresponding frazil event. The statistics (sample number, N, correlation coefficient, R, and t value) are indicated at the bottom right of each panel except (E), where $P < 0.001$ (correlation is significant at the 0.001 level) for all the cases.

The mean flow directions at a1 and a2 (indicated by arrows in Fig. 1A) roughly follow the bottom contours. The flow is stably directed to the mean flow direction (Fig. 2I) with the dominance of the barotropic component and interpreted as part of the westward Antarctic Coastal Current. However, the current speed at a1 is slower than that at a2, particularly from late May to July. In the polynya, a water column with a slower speed has a longer residence time and can accumulate a large salt input. The longer and larger salinity increase at a1 is likely due to the longer residence time in the high ice production region. Taking advantage of having the daily ice production dataset, we show these effects in a simple demonstrative calculation.

We assume that the entire water mass moves barotropically along the bottom contour at the same speed as the dominant velocity component at a1 and a2 (Fig. 2I). Specifically, the water mass is assumed to come from the east along the blue and purple lines in Fig. 1A. Under this assumption, the salinity increase in the water mass is determined by integrating brine rejection due to ice production at the backward-tracked position along the lines. Hence, we calculated the salinity increase in shelf water using daily sea ice production, referred to as the backward-tracking experiment (see Materials and Methods).

The results are superimposed in Fig. 2 (E and F) as purple lines (enlarged in fig. S7). The calculated salinity variations are similar to the observed variations for both a1 and a2. In the case of a1, a slower velocity and a longer trajectory route result in a longer residence time of ~2 to 3 months in the high–ice production area. Thus, the water column could accumulate a large salt input for 2 to 3 months from the start of ice production. The salinity increase stops when the ice production period exceeds the residence time. In contrast, the water column coming to a2 has a much shorter residence time (~1 month) owing to a higher velocity and a shorter trajectory route, and its salinity only increases during the initial ~1 month. The salinity variation caused by local sea ice production (dotted purple lines) explains the salinity increases at both sites only at the initial stage, when the local salinity budget can be approximated. Although our method is rough and, in reality, the water column would not exactly follow the bottom contours, disturbed by time-varying eddies, etc. (38), it demonstrates the importance of the residence time on the salinity increase. A large salinity increase does not occur at a2 with a higher local ice production of 15.5 m/year (Fig. 1A) and a shorter residence time, while it occurs at a1 with a slightly lower ice production of 13.9 m/year and a longer residence time, which results in DSW formation only at a1.

DSW formation leading to AABW

Next, we discuss how brine rejection by sea ice production leads to DSW/AABW formation. From May to June, the upper and lower layers at a2 exhibit coherent variations (Fig. 2, F and G). However, beginning early in July, high-salinity water with potential supercooling appears

sporadically only in the lower layer. Its salinity increases gradually from July to September, exhibiting a density similar to that of a1 (Fig. 2H). These sporadic changes at a2 can be interpreted as a DSW intruding from the nearshore region, where higher-salinity water is formed, as shown in a1. In addition, warmer water sporadically appears in the lower layer at a2 after late August; this water is thought to originate from mCDW.

To examine the water mass properties in terms of CDBW formation, we use a potential temperature-salinity (θ-S) diagram (Fig. 4). The monthly averaged values are plotted for the a1 and a2 upper layers. From June through September, the salinity at a1 increases to 34.6 to 34.8, dense enough to be the CDBW source. Although the upper layer at a2 is not dense enough, plots of the lower layer at a2 in late winter (red dots in Fig. 4 corresponding to the time indicated by the orange bar in Fig. 2G) are distributed along the mixing line of CDBW that is formed by the mixing of mCDW and pure DSW.

From these behaviors, the following processes can be inferred. DSW formed in the nearshore region subducts into the lower layer of the offshore shelf region and then descends the shelf slope, inducing the compensating onshore-ward flow of mCDW, as represented in the model simulation (21, 22). The offshore-ward DSW and onshore-ward mCDW would be mixed to form the CDBW. Figure 5 summarizes the seasonal evolution of water mass formation associated with underwater frazil ice production.

DISCUSSION

Implications of the dominant underwater frazil ice

Our acoustic observations provide a valuable validation of the AMSR algorithm (26) for detecting active-frazil areas (Figs. 2 and 3). However, the satellite can only capture the surface conditions of ice or ocean and cannot directly measure underwater frazil ice. On the other hand, the penetration depth of frazil ice is found to be closely related to wind speed (Fig. 3D). Here, we seek a method in which deep-penetrating frazils are inferred from wind and satellite product information. If we consider a frazil penetration deeper than 30 m, among all the occurrences of this deep frazil penetration, more than 80% occur at wind speeds higher than 15 m s^{-1}, about 70% occur at an active-frazil ratio of more than 50%, and about 70% occur at a sea ice production larger than 9 cm/day (fig. S8). If the wind speed is greater than 15 m s^{-1} and the active-frazil ratio is greater than 50%, then deep frazil penetration occurs at a rate greater than 95%. Therefore, the combined information of the wind and satellite AMSR enables the detection of deep frazil penetration to some extent, at least for the CDP.

We regarded an active-frazil area by the AMSR algorithm with a wind speed of >15 m s^{-1} as an index of deep frazil penetration. We then mapped its mean occurrence rate over the entire Southern Ocean during the freezing period (Fig. 6). Although the properties of shelf water and the geographic situation in each polynya may also affect deep frazil formation, the map suggests that deep frazil is prominent particularly in the CDP. This is probably because the offshore-ward wind dominates in the CDP with high speeds (purple sticks in Fig. 2A). Sea ice production associated with deep frazil is also the largest at the CDP (table S2), which makes the CDP a source area of AABW formation among the Antarctic coastal polynyas. On the other hand, the map suggests that a deep frazil also occurs in other polynyas. Considering recent observations of frequently occurring supercooled water in Antarctic coastal waters (24, 25), it is likely
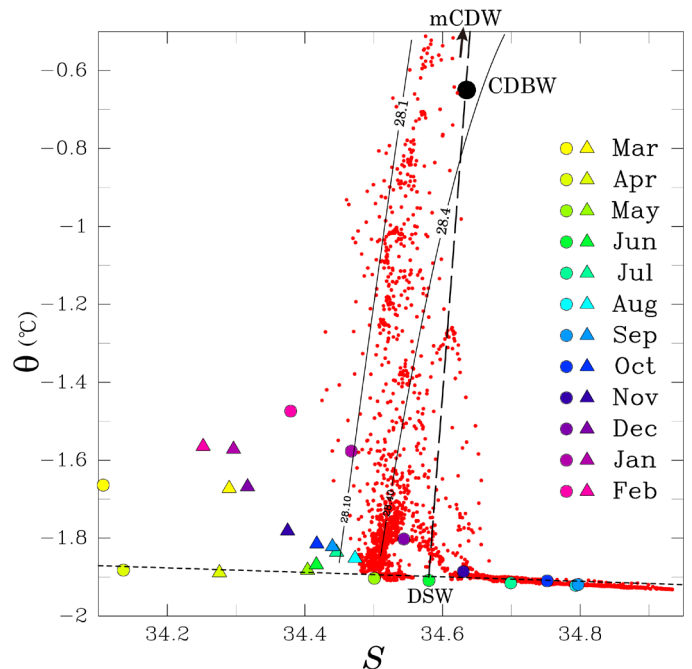

Fig. 4. Potential temperature-salinity (θ-S) diagram for mooring data. The monthly mean water properties are represented as circles for a1 and triangles for the upper layer at a2, color-coded by month. Red dots represent the lower layer at a2 at 6-hour intervals from August 20 to September 10. The mean θ and S of the CDBW outflow obtained from Ohshima et al. (7) is denoted by the solid black circle. The mixing line of CDBW connecting mCDW to pure (freezing point) DSW is shown as a dashed line. The freezing temperature line is shown as a dotted line. Isolines of neutral density (kg m^{-3}) are given as thin black curves.

that deep-penetrating frazil ice occasionally occurs in other Antarctic coastal polynyas where the strong wind and severe cooling conditions occur. Such a fact has probably been missed because of logistic difficulties in direct observations.

In addition to high ice production, deep-penetrating frazil ice potentially plays an important role in the transport of particulate matter. When it reaches the bottom or gets in contact with resuspended sediments, it can incorporate sediments or macronutrients such as iron (30, 39–41), which are then transported by ice floes and released when the ice melts (41), possibly leading to high biological productivity (42). Alternatively, frazil ice could itself induce algal blooms as green frazil ice in major Antarctic polynyas, among which the CDP is one of the most active areas of frazil ice–associated algal production (43, 44). This might be related to the fact that the CDP is the most prominent area of deep frazil ice. As such, dominant frazil ice could potentially contribute to high biological productivity in the Southern Ocean.

The most important finding of this study is the frequent occurrence of deep penetration of frazil ice down to 80 m or more in the CDP. The widely accepted concept of a coastal polynya proposes that thin-ice or open-water areas are maintained by offshore advection of newly formed ice and that accumulation and consolidation of advected new ice at the polynya edge limits the polynya extent/ice production (45, 46). Our observations instead suggest that as long as strong winds continue (typically >15 m s^{-1}), underwater frazil ice formation persistently occurs, and a mixture of frazil ice streaks and open water can be maintained at the surface without accumulation
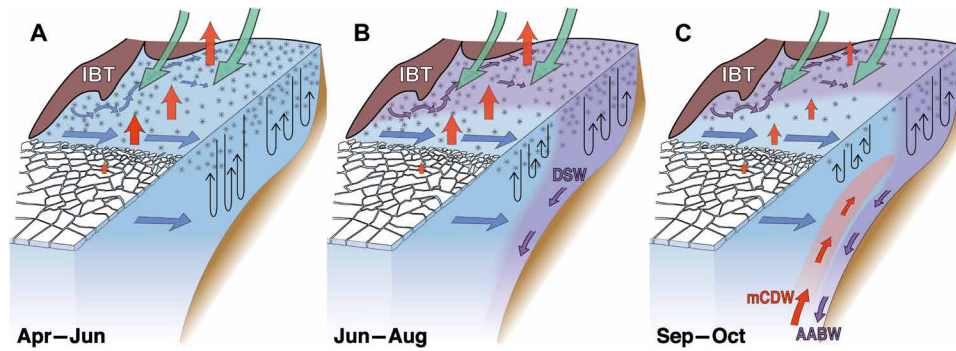
Fig. 5. Seasonal evolution of underwater frazil ice production in the CDP and associated DSW/AABW formation. (**A**) From late March through June, strong wind events induce underwater frazil ice formation (designated by *) with potential supercooling. Dominant frazil ice production causes active brine rejection with deepening of the winter mixed layer. (**B**) From June through August, the water mass in the nearshore region, which has a relatively long residence time in the polynya area, increases in salinity and density (colored by purple). In contrast, the water mass near the shelf edge, which has a shorter residence time, stops increasing in salinity by June. This difference creates a large density difference between the nearshore and offshore shelf, causing sporadic intrusion of the nearshore DSW into the lower layer in the offshore shelf. A clear stratification is then formed in the offshore shelf, which prevents the deepening of the winter mixed layer. (**C**) From late August through October, DSW lastly descends down the shelf slope, inducing the compensating onshore-ward flow of mCDW. Hence, DSW and mCDW mix, concentrate along the canyon, and gradually create new AABW, i.e., CDBW. IBT represents the grounded iceberg tongue.

of heat-insulating thick ice. This creates an efficient ice production system in the polynyas. Combined with the skimming effect of the grounded iceberg tongue upstream of the polynya (*47*), this mechanism induces higher ice production in the CDP than previous estimates (*36*, *37*), leading to AABW formation. Combined observations of the water properties and current velocity with sea ice production suggest that the residence time in the polynya is another key factor for DSW/AABW formation. DSW formation occurs only in the nearshore with longer residence times in the high ice production region, although the ice production in the offshore is comparably high. Last, our findings of dominantly formed deep frazil ice and subsequent processes in the polynya should be better represented in future modeling studies of DSW/AABW formation.

MATERIALS AND METHODS
ADCP backscatter strength measurement
ADCPs measured the acoustic backscatter strength at 15-min intervals with a cell length set to 8 m. The bin ranges are summarized in table S1. The dynamic range is ±80 dB, and the accuracy of the echo intensity is ±1.5 dB. The acoustic frequency of the emitted ping is 307 kHz, corresponding to a 5-mm wavelength. Processing the backscatter strength from the ADCPs followed our previous studies (*30*, *31*, *48*–*50*). The ADCP emits and receives acoustic pings with the same transducer. The acoustic pressure of the received ping is amplified and converted to an 8-bit digitized electric voltage amplitude in counts, called the echo amplitude. The echo intensity received by the transducer depends on the distance from the transducer to scatterers because of geometric spreading of the acoustic beam and sound absorption by the water. Because the echo amplitude is determined by distance-dependent transmission loss and battery power, different distance bins and times cannot be compared.

To correct for these effects, we used the target strength per unit volume in dB, called the volume backscatter strength, SV, which is calculated from the sonar Eq. 1 as follows

$$SV = k_c(E - E_r) + 2\alpha Di + 20 \log_{10} Di + 10 \log_{10} \frac{T_x}{LW_t} + C \quad (1)$$

where $k_c = 0.45$ (dB counts^{-1}) is the conversion coefficient, E (counts) is the echo amplitude, E_r (counts) is the received noise, α (dB m^{-1}) is the attenuation coefficient, and Di (m) is the distance between the transducer and the central depth of each bin i ($i = 1, 2, 3, \ldots$) along the acoustic beam. T_x (K) is the transducer temperature, L (m) is the pulse length, W_t (W) is the transmit power, and $C = -143.5$ (dB) is a constant. E_r is derived from the echo amplitude before deployment and was 41. L was set to 8.26 m for a1 and 8.28 m for a2. The transducer temperature, T_x, was obtained from the ADCP temperature sensor. W_t was calculated using the electric voltage and current recorded by the instrument for every measurement. α is determined from the sum of the terms of the acoustic absorption by seawater and scattering and/or absorption by suspended matter. As in previous studies (*48*, *49*), the latter effect was ignored, and α was assumed to be 0.069 dB m^{-1}.

There are several candidates as the acoustic scatterers in the water column, for example, air bubbles, marine organisms such as zooplankton, and resuspended sediment, as well as frazil ice. In December and January, when the ocean was heated by the atmosphere (shortwave radiation) and the water temperature was notably higher than the freezing point at a1, no penetrating underwater scatter has ever been detected by the ADCP, even with high wind speeds of 10 to 20 m s^{-1}. Therefore, the deep-penetrating acoustic signals that occurred in windy winter conditions cannot be explained by air bubbles. In general, zooplankton move to the ocean bottom during the day and return to the surface during the night [e.g., (*51*)]. Such a diurnal cycle can be found for some time periods at a2 (Fig. 2D and fig. S6D). Except for these diurnal signals, most of the observed backscatter signals are regarded as those from underwater frazil ice.

Supercooling
Supercooling occurs when the water temperature is less than the freezing point (in situ supercooling). The freezing point, T_f, is estimated from the UNESCO algorithm (*52*) using the salinity, S, and water pressure, P_w (Pa), as

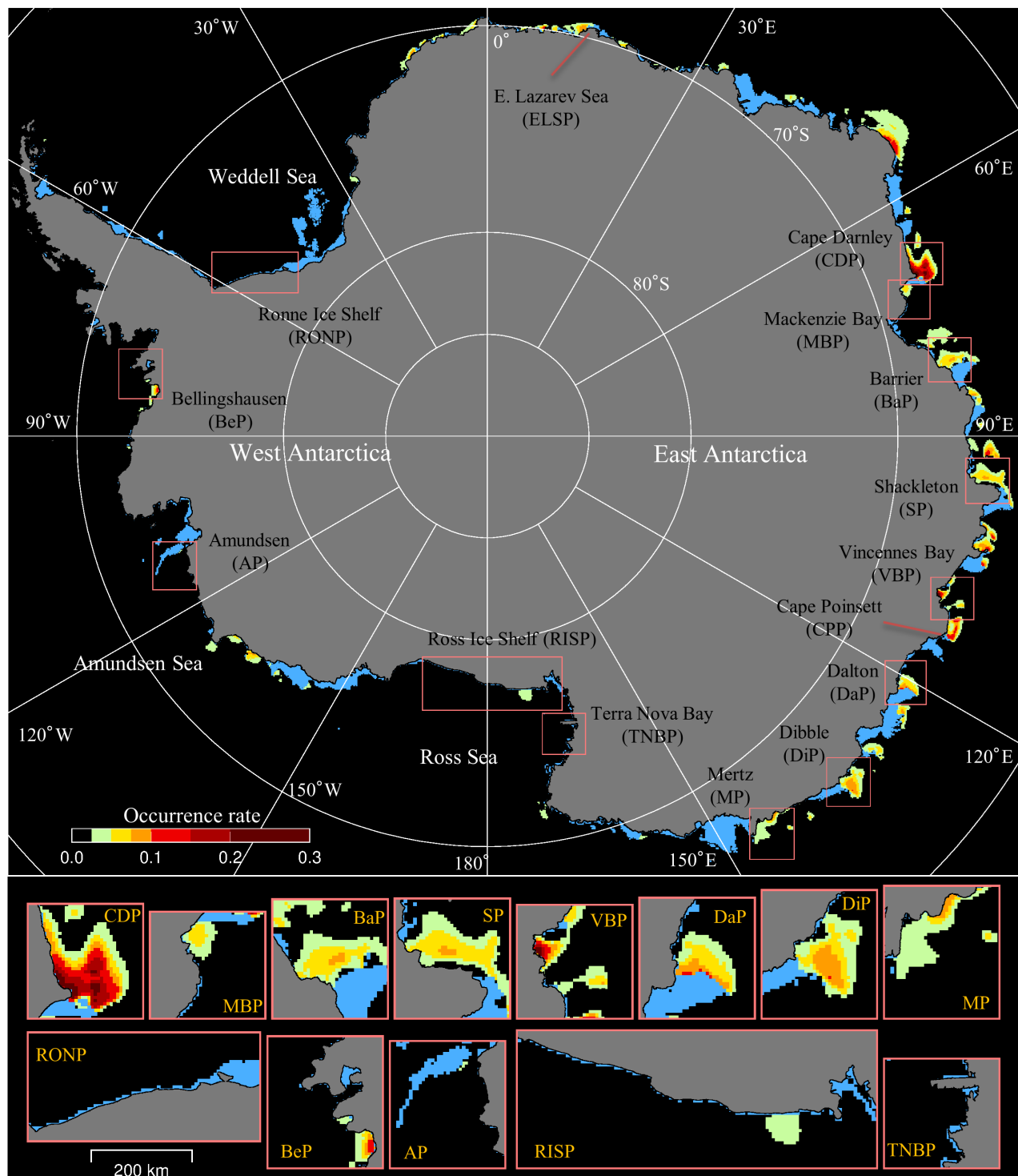$$T_f(S, P_w) = a_1 S + a_2 S^{3/2} + a_3 S^2 + bP_w \quad (2)$$

Fig. 6. Map of the mean occurrence rate of an index of deep-penetrating frazil ice over the entire Southern Ocean. An active-frazil area detected by the AMSR algorithm with a wind speed of >15 m s^{-1} is assumed to be a good index for a region of deep penetration (typically >30 m) of frazil ice. The analysis was made during the freezing period (March–November) for 2003–2010. Areas of landfast sea ice with an occurrence rate of >55% detected by AMSR (*36*) are shown in blue. The bottom figures are close-up maps of the major coastal polynyas designated by pink boxes. Polynya names follow Nakata *et al.* (*27*), and their abbreviations are shown in parentheses. Detection of the active-frazil area was based on the AMSR ice-type classification algorithm (*26*).

where $a_1 = -0.0575°C$, $a_2 = 1.710532 \times 10^{-3}°C$, $a_3 = -2.154996 \times 10^{-4}°C$, and $b = -7.53 \times 10^{-8}°C/Pa$. T_f derived from Eq. 2 has an error of at least ±2 mK. According to Eq. 2, the freezing point decreases with depth (~7.5 mK/10 m). Potential supercooling is attained when the potential temperature is below the freezing point at the surface estimated as $T_f (S, 0)$. Potentially supercooled water becomes supercooled if it is raised adiabatically to the surface.

This study assesses potential supercooling at the depth of the CT recorder. Taking into account the accuracy of the water temperature, potential temperature, salinity, water pressure, and Eq. 2, T_f can be estimated with an error of ±6 mK. The potential supercooling presented in Fig. 2 (E to G) (light blue shading) should be interpreted with caution because the magnitude of observed potential supercooling (~10 mK) is a similar magnitude as the instrument error (~6 mK). However, all three CT recorders showed similar magnitudes of potential supercooling. Furthermore, when the surface mixed layer reached the lower layer at a2 during May–June, the CT recorders in the upper and lower layers show the supercooling of similar magnitudes coherently in accordance with the strong wind events. We therefore conclude that the potential supercooling with suspended frazil ice likely occurs.

Estimation of sea ice production with classification of ice type from AMSR

Thin-ice (polynya) areas can be roughly classified into two ice types: active frazil (which is a frazil/grease/pancake ice area formed in turbulent conditions) and thin solid ice (which is a nilas or gray ice: a nearly uniform, thin ice-covered area formed in calm conditions). We classified the sea ice region into thick ice, thin solid ice, and active frazil with an ice-type classification algorithm of the Advanced Microwave Scanning Radiometer for the Earth Observing System (AMSR-E) (26). In this algorithm, thin ice regions are classified into active frazil and thin solid ice using a linear discriminant function of the polarization ratio at 36 GHz and the gradient ratio at 36 and 89 GHz. We have compared the results of the ice-type classification algorithm with many synthetic aperture radar images in the major Antarctic coastal polynya, showing some examples in fig. S9. We have confirmed that the AMSR algorithm reliably detects active-frazil areas, which are represented by high backscatter streaks in the radar images.

Once the AMSR pixel is classified as active frazil or thin solid ice, the ice thickness is derived from the polarization ratio–ice thickness relationship, separately given for active frazil and thin solid ice. The ice type and ice thickness are interpolated onto the National Snow and Ice Data Center polar stereographic grid with a spatial resolution of 12.5 km.

We estimated sea ice production, using these ice thickness data for the periods of AMSR-E (2003–2010) and AMSR2 (2013–2019). The procedure of the estimation basically followed Ohshima et al. (53). We assumed that sea ice production occurs only in the grid cells assigned as areas of thin ice by the algorithm. Under the assumption that all heat loss at the surface goes toward freezing, the volume of ice production (V) is given by $V = Q / (\rho_i L_f)$, where Q is the heat loss at the ice surface, ρ_i (= 920 kg m^{-3}) is the ice density, and L_f (= 0.334 MJ kg^{-1}) (23) is the latent heat of fusion of sea ice. Heat loss is obtained from the assumption that the sum of radiative and turbulent fluxes at the ice surface is balanced by the conductive heat flux through the ice. The thermal inertia of ice is neglected because its contribution to the net heat flux is small for thin ice under typical meteorological conditions during the winter.

In reality, sea ice thickness is not uniform in a microwave footprint. The AMSR thin-ice algorithm (26) uses thermal ice thickness, which is defined as the thickness for which the calculated total heat flux would be realized if the ice thickness were uniform in the microwave footprint. This thickness is suitable for calculating heat flux and thus sea ice production (54). Particularly for the active-frazil areas, where frazil/grease/pancake ice and open water are mixed, physical ice thickness is hard to define, while thermal ice thickness can be defined and used for the calculation of sea ice production. It should be noted that active-frazil areas generally have much smaller thermal ice thickness than thin solid-ice areas do, which causes higher ice production in the active-frazil areas.

Sensible and latent heat fluxes were calculated from the bulk formula (55). Longwave radiation and shortwave radiation were calculated from the empirical formula as in the study by Nakata et al. (27). Shortwave radiation was assumed to be completely absorbed in the thin surface layer (not transmitted into the ice interior). The surface albedo of thin ice was set to 0.36 for the thickness range 0.1 to 0.2 m and to 0.27 for the thickness range 0.0 to 0.1 m (56, 57).

The net longwave radiation and turbulent (sensible and latent) heat fluxes are functions of the surface temperature of sea ice, T_s. The conductive heat flux through the ice, F_c, is also a function of T_s when the ice thickness, h_i, is known and the ice bottom temperature is assumed to be the freezing point of seawater, T_f (no oceanic heat flux). The value of T_s can then be obtained so that the sum of all the flux components is zero (balanced) at the ice surface. Once T_s is obtained, the conductive heat flux, F_c, corresponding to the heat loss, is calculated from $F_c = k_i (T_f - T_s)/h_i$, where k_i (= 2.03 W m^{-1} K^{-1}) is the thermal conductivity of sea ice. As input surface atmospheric data, we used the European Centre for Medium-Range Weather Forecasts (ECMWF) ERA5 data with 0.25° × 0.25° spatial resolution and 1-hour temporal resolution.

For mapping and estimation of ice type (Figs. 1B and 6 and figs. S3, S5, and S9) and ice production (Fig. 1A and figs. S1 to S3), regions of land and landfast sea ice were masked out using the land and landfast ice mask data with a resolution of ~6.25 km, obtained from the fast-ice detection algorithm (36). We also masked out regions with ice concentrations less than 30% as open-water areas using the enhanced NASA Team algorithm (NT2) (58) with a spatial resolution of 12.5 km.

Backward-tracking experiment to calculate salinity increase

We calculate the salinity increase in shelf water associated with brine rejection using the daily sea ice production H (represented by ice thickness) in an area A with the water column thickness of D, based on the salt budget. According to Cavalieri and Martin (59), the salt flux by the daily ice production, F_0, is given by

$$F_0 = (0.69 \times 10^{-3})\rho_i A H S_0 \quad (3)$$

where ρ_i (= 920 kg m^{-3}) is the sea ice density and S_0 is the initial salinity of shelf water. From the conservation of salinity, the salinity increase of shelf water, ΔS, caused by the salt flux associated with F_0 is given by

$$\Delta S = (F_0 \times 10^3)/(AD\rho_0) \quad (4)$$

where ρ_0 (= 1030 kg m^{-3}) is the water density. Combining Eqs. 3 and 4 gives

$$\Delta S \ = \ 0.69 \times (\rho_i H)/(\rho_0 D) \times S_0 \qquad (5)$$

The salinity input by ice production was assumed to distribute evenly in the whole water column in the case of a1. This assumption was based on our observation that potential supercooling at a depth of 128 m (CT recorder) was maintained throughout the winter and the observation at almost the same location as a1 in 2017 (*60*) that salinity changes occurred similarly throughout the whole water column. These facts suggest that the surface mixed layer reaches the bottom throughout the winter at a1.

In the case of a2, the salinity and density of the upper layer were lower than those of the lower layer in March and April (Fig. 2, F to H), showing that the surface mixed layer did not reach the lower layer. In May and June, the salinity and density of the upper and lower layers coincided, implying that the mixed layer reached the lower layer. However, after late June, high-salinity and dense water occasionally appeared only in the lower layer, forming a clear stratification against the upper layer. On the basis of these observations, the bottom of the surface mixed layer was set at the midpoint between the depths of the upper and lower CT recorders, 156 m. For simplicity, the salinity input by ice production is assumed to be used in this mixed layer.

For the backward-tracking calculation, we set the start date as April 1 for a1 and April 9 for a2 and the initial salinity, S_0, as 34.0 for a1 and 34.22 for a2. The trajectory routes for upstream integration were assumed to end at the front of the Amery Ice Shelf. The salinity results from the method are presented as purple lines in Fig. 2 (E and F) and fig. S7. Because the reality deviates from the simple assumption (following the bottom contours with the same speed as that at the mooring site) because of time-varying eddies, etc., the longer integration leads to larger ambiguity. The results are shown by the middle of August, when the eddy activity likely increases owing to the intrusion of the warmer water (see Fig. 2G).

SUPPLEMENTARY MATERIALS

Supplementary material for this article is available at https://science.org/doi/10.1126/sciadv.adc9174

REFERENCES AND NOTES

1. A. H. Orsi, G. C. Johnson, J. L. Bullister, Circulation, mixing, and production of Antarctic Bottom Water. *Prog. Oceanogr.* **43**, 55–109 (1999).
2. G. C. Johnson, Quantifying Antarctic Bottom Water and North Atlantic Deep Water volumes. *J. Geophys. Res.* **113**, C05027 (2008).
3. S. G. Purkey, G. C. Johnson, Antarctic Bottom Water warming and freshening: Contributions to sea level rise, ocean freshwater budgets, and global heat gain. *J. Climate* **26**, 6105–6122 (2013).
4. S. R. Rintoul, in *Ocean, Ice, and Atmosphere: Interactions at the Antarctic Continental Margin*, S. S. Jacobs, R. F. Weiss, Eds. (Antarctic Research Series, American Geophysical Union, 1998), vol. 75, pp. 151–171.
5. G. D. Williams, N. L. Bindoff, S. J. Marsland, S. R. Rintoul, Formation and export of dense shelf water from the Adélie Depression, East Antarctica. *J. Geophys. Res.* **113**, C04039 (2008).
6. T. Tamura, K. I. Ohshima, S. Nihashi, Mapping of sea-ice production for Antarctic coastal polynyas. *Geophys. Res. Lett.* **35**, L07606 (2008).
7. K. I. Ohshima, Y. Fukamachi, G. D. Williams, S. Nihashi, F. Roquet, Y. Kitade, T. Tamura, D. Hirano, L. Herraiz-Borreguero, I. Field, M. Hindell, S. Aoki, M. Wakatsuchi, Antarctic Bottom Water production by intense sea-ice formation in the Cape Darnley polynya. *Nat. Geosci.* **6**, 235–240 (2013).
8. M. P. Meredith, Replenishing the abyss. *Nat. Geosci.* **6**, 166–167 (2013).
9. M. P. Meredith, R. A. Locarnini, K. A. Van Scoy, A. J. Watson, K. J. Heywood, B. A. King, On the sources of Weddell Gyre Antarctic Bottom Water. *J. Geophys. Res.* **105**, 1093–1104 (2000).
10. M. P. Couldrey, L. Jullion, A. C. N. Garabato, C. Rye, L. Herráiz-Borreguero, P. J. Brown, M. P. Meredith, K. L. Speer, Remotely induced warming of Antarctic bottom water in the eastern Weddell Gyre. *Geophys. Res. Lett.* **40**, 2755–2760 (2013).
11. L. Jullion, A. C. N. Garabato, S. Bacon, M. P. Meredith, P. J. Brown, S. Torres-Valdés, K. G. Speer, P. R. Holland, J. Dong, D. Bakker, M. Hoppema, B. Loose, H. J. Venables, W. J. Jenkins, M.-J. Messias, E. Fahrbach, The contribution of the Weddell Gyre to the lower limb of the global overturning circulation. *J. Geophys. Res.* **119**, 3357–3377 (2014).
12. A. P. S. Wong, S. C. Riser, Modified shelf water on the continental slope north of Mac Robertson Land, East Antarctica. *Geophys. Res. Lett.* **40**, 6186–6190 (2013).
13. G. Mizuta, Y. Fukamachi, D. Simizu, Y. Matsumura, Y. Kitade, D. Hirano, M. Fujii, Y. Nogi, K. I. Ohshima, Seasonal evolution of Cape Darnley bottom water revealed by mooring measurements. *Front. Mar. Sci.* **8**, 657119 (2021).
14. D. Hirano, Y. Kitade, K. I. Ohshima, Y. Fukamachi, The role of turbulent mixing in the modified shelf water overflows that produce Cape Darnley bottom water. *J. Geophys. Res.* **120**, 910–922 (2015).
15. K. Murakami, D. Nomura, G. Hashida, S. Nakaoka, Y. Kitade, D. Hirano, T. Hirawake, K. I. Ohshima, Strong biological carbon uptake and carbonate chemistry associated with dense shelf water outflows in the Cape Darnley polynya, East Antarctica. *Mar. Chem.* **225**, 103842 (2020).
16. Y. Ohashi, M. Yamamoto-Kawai, K. Kusahara, K. Sasaki, K. I. Ohshima, Age distribution of Antarctic Bottom Water off Cape Darnley, East Antarctica, estimated using chlorofluorocarbon and sulfur hexafluoride. *Sci. Rep.* **12**, 8462 (2022).
17. S. Aoki, K. Katsumata, M. Hamaguchi, A. Noda, Y. Kitade, K. Shimada, D. Hirano, D. Simizu, Y. Aoyama, K. Doi, Y. Nogi, Freshening of Antarctic Bottom Water off Cape Darnley, East Antarctica. *J. Geophys. Res.* **125**, e2020JC016374 (2020).
18. L. Gao, Y. Zu, G. Guo, S. Hou, Recent changes and distribution of the newly-formed Cape Darnley Bottom Water, East Antarctica. *Deep-Sea Res. II* **201**, 105119 (2022).
19. Y. Nakayama, K. I. Ohshima, Y. Matsumura, Y. Fukamachi, H. Hasumi, A numerical investigation of formation and variability of Antarctic bottom water off Cape Darnley, East Antarctica. *J. Phys. Oceanogr.* **44**, 2921–2937 (2014).
20. V. Mensah, Y. Nakayama, M. Fujii, Y. Nogi, K. I. Ohshima, Dense water downslope flow and AABW production in a numerical model: Sensitivity to horizontal and vertical resolution in the region off Cape Darnley polynya. *Ocean Model.* **165**, 101843 (2021).
21. A. K. Morrison, A. M. Hogg, M. H. England, P. Spence, Warm circumpolar deep water transport toward Antarctica driven by local dense water export in canyons. *Sci. Adv.* **6**, eaav2516 (2020).
22. R. Moorman, A. K. Morrison, A. M. Hogg, Thermal responses to Antarctic ice shelf melt in an eddy-rich global ocean–sea ice model. *J. Climate* **33**, 6599–6620 (2020).
23. S. Martin, Frazil ice in rivers and oceans. *Annu. Rev. Fluid Mech.* **13**, 379–397 (1981).
24. L. Thompson, M. Smith, J. Thomson, S. Stammerjohn, S. Ackley, B. Loose, Frazil ice growth and production during katabatic wind events in the Ross Sea, Antarctica. *Cryosphere* **14**, 3329–3347 (2020).
25. F. A. Haumann, R. Moorman, S. C. Riser, L. H. Smedsrud, T. Maksym, A. P. S. Wong, E. A. Wilson, R. Drucker, L. D. Talley, K. S. Johnson, R. M. Key, J. L. Sarmiento, Supercooled Southern Ocean waters. *Geophys. Res. Lett.* **47**, e2020GL090242 (2020).
26. K. Nakata, K. I. Ohshima, S. Nihashi, Estimation of thin ice thickness and discrimination of ice type from AMSR-E passive microwave data. *IEEE Trans. Geosci. Remote Sens.* **57**, 263–276 (2019).
27. K. Nakata, K. I. Ohshima, S. Nihashi, Mapping of active frazil for Antarctic coastal polynyas, with an estimation of sea-ice production. *Geophys. Res. Lett.* **48**, e2020GL091353 (2021).
28. R. Drucker, S. Martin, R. Moritz, Observations of ice thickness and frazil ice in the St. Lawrence Island polynya from satellite imagery, upward looking sonar, and salinity/temperature moorings. *J. Geophys. Res.* **108**, 3149 (2003).
29. I. A. Dmitrenko, C. Wegner, H. Kassens, S. A. Kirillov, T. Krumpen, G. Heinemann, A. Helbig, D. Schröder, J. A. Hölemann, T. Klagge, K. P. Tyshko, T. Busche, Observations of supercooling and frazil ice formation in the Laptev Sea coastal polynya. *J. Geophys. Res.* **115**, C08010 (2010).
30. M. Ito, K. I. Ohshima, Y. Fukamachi, D. Hirano, A. R. Mahoney, J. Jones, T. Takatsuka, H. Eicken, Favorable conditions for suspension freezing in an Arctic coastal polynya. *J. Geophys. Res.* **124**, 8701–8719 (2019).
31. M. Ito, Y. Fukamachi, K. I. Ohshima, K. Shirasawa, Observational evidence of supercooling and frazil ice formation throughout the water column in a coastal polynya in the Sea of Okhotsk. *Cont. Shelf Res.* **196**, 104072 (2020).
32. G. Dieckmann, G. Rohardt, H. Hellmer, J. Kipfstuhl, The occurrence of ice platelets at 250 m depth near the Filchner Ice Shelf and its significance for sea ice biology. *Deep-Sea Res.* **33**, 141–148 (1986).
33. J. D. Penrose, M. Conde, T. J. Pauly, Acoustic detection of ice crystals in Antarctic waters. *J. Geophys. Res.* **99**, 12573–12580 (1994).
34. P. J. Langhorne, K. G. Hughes, A. J. Gough, I. J. Smith, M. J. M. Williams, N. J. Robinson, C. L. Stevens, W. Rack, D. Price, G. H. Leonard, A. R. Mahoney, C. Haas, T. G. Haskell,

Observed platelet ice distributions in Antarctic sea ice: An index for ocean-ice shelf heat flux. *Geophys. Res. Lett.* **42**, 5442–5451 (2015).

35. G. M. Brett, A. Irvin, W. Rack, C. Haas, P. J. Langhorne, G. H. Leonard, Variability in the distribution of fast ice and the sub-ice platelet layer near McMurdo Ice Shelf. *J. Geophys. Res.* **125**, e2019JC015678 (2020).

36. S. Nihashi, K. I. Ohshima, Circumpolar mapping of Antarctic coastal polynyas and landfast sea ice: Relationship and variability. *J. Climate* **28**, 3650–3670 (2015).

37. T. Tamura, K. I. Ohshima, A. D. Fraser, G. D. Williams, Sea ice production variability in Antarctic coastal polynyas. *J. Geophys. Res.* **121**, 2967–2979 (2016).

38. A. L. Stewart, A. F. Thompson, Eddy generation and jet formation via dense water outflows across the Antarctic continental slope. *J. Phys. Oceanogr.* **46**, 3729–3750 (2016).

39. L. H. Smedsrud, Frazil-ice entrainment of sediment: Large-tank laboratory experiments. *J. Glaciol.* **47**, 461–471 (2001).

40. M. Ito, K. I. Ohshima, Y. Fukamachi, G. Mizuta, Y. Kusumoto, J. Nishioka, Observations of frazil ice formation and upward sediment transport in the Sea of Okhotsk: A possible mechanism of iron supply to sea ice. *J. Geophys. Res.* **122**, 788–802 (2017).

41. H. Eicken, R. Gradinger, A. Gaylord, A. Mahoney, I. Rigor, H. Melling, Sediment transport by sea ice in the Chukchi and Beaufort Seas: Increasing importance due to changing ice conditions? *Deep Sea Res. II* **52**, 3281–3302 (2005).

42. P. N. Sedwick, G. R. DiTullio, Regulation of algal blooms in Antarctic shelf waters by the release of iron from melting sea ice. *Geophys. Res. Lett.* **24**, 2515–2518 (1997).

43. J. L. Lieser, M. A. J. Curran, A. R. Bowie, A. T. Davidson, S. J. Doust, A. D. Fraser, B. K. Galton-Fenzi, R. A. Massom, K. M. Meiners, J. Melbourne-Thomas, P. A. Reid, P. G. Strutton, T. R. Vance, M. Vancoppenolle, K. J. Westwood, S. W. Wright, Antarctic slush-ice algal accumulation not quantified through conventional satellite imagery: Beware the ice of March. *Cryosphere* **9**, 6187–6222 (2015).

44. H. B. DeJong, R. B. Dunbar, E. A. Lyons, Late summer frazil ice-associated algal blooms around Antarctica. *Geophys. Res. Lett.* **45**, 826–833 (2018).

45. C. H. Pease, The size of wind-driven coastal polynyas. *J. Geophys. Res.* **92**, 7049–7059 (1987).

46. M. A. Morales Maqueda, A. J. Willmott, N. R. T. Biggs, Polynya dynamics: A review of observations and modeling. *Rev. Geophy.* **42**, RG1004 (2004).

47. A. D. Fraser, K. I. Ohshima, S. Nihashi, R. A. Massom, T. Tamura, K. Nakata, G. D. Williams, S. Carpentier, S. Willmes, Landfast ice controls on sea-ice production in the Cape Darnley Polynya: A case study. *Remote Sens. Environ.* **233**, 111315 (2019).

48. K. L. Deines, Backscatter estimation using broadband acoustic Doppler current profilers, in *Proceedings of the IEEE Sixth Working Conference on Current Measurement (Cat. No.99CH36331)*, San Diego, CA, 13 March 1999 (IEEE, 1999), pp. 249–253.

49. A. J. F. Hoitink, Tidally-induced clouds of suspended sediment connected to shallow-water coral reefs. *Mar. Geol.* **208**, 13–31 (2004).

50. M. Ito, K. I. Ohshima, Y. Fukamachi, G. Mizuta, Y. Kusumoto, T. Kikuchi, Underwater frazil ice and its suspension depth detected from ADCP backscatter data around sea ice edge in the Sea of Okhotsk. *Cold Reg. Sci. Technol.* **192**, 103382 (2021).

51. V. Petrusevich, I. A. Dmitrenko, S. A. Kirillov, S. Rysgaard, S. Falk-Petersen, D. G. Barber, W. Boone, J. K. Ehn, Wintertime water dynamics and moonlight disruption of the acoustic backscatter diurnal signal in an ice-covered Northeast Greenland fjord. *J. Geophys. Res.* **121**, 4804–4818 (2016).

52. N. P. Fofonoff, R. C. Millard Jr., Algorithms for the computation of fundamental properties of seawater. *UNESCO Tech. Pap. Mar. Sci.* **44**, 1–53 (1983).

53. K. I. Ohshima, T. Watanabe, S. Nihashi, Surface heat budget of the Sea of Okhotsk during 1987-2001 and the role of sea ice on it. *J. Meteorol. Soc. Jpn.* **81**, 653–677 (2003).

54. H. Kashiwase, K. I. Ohshima, Y. Fukamachi, S. Nihashi, T. Tamura, Evaluation of AMSR-E thin ice thickness algorithm from a mooring-based observation: How can the satellite observe a sea ice field with nonuniform thickness distribution? *J. Atmos. Oceanic Tech.* **36**, 1623–1641 (2019).

55. J. Kondo, Air-sea bulk transfer coefficients in diabatic conditions. *Bound.-Layer Meteor.* **9**, 91–112 (1975).

56. G. A. Maykut, The surface heat and mass balance, in *The Geophysics of Sea Ice*, N. Untersteiner, Ed. (NATO ASI Series, Springer, 1986), pp. 395–463.

57. I. Allison, R. E. Brandt, S. G. Warren, East Antarctic sea ice: Albedo, thickness distribution, and snow cover. *J. Geophys. Res.* **98**, 12417–12429 (1993).

58. T. Markus, D. J. Cavalieri, An enhancement of the NASA Team sea ice algorithm. *IEEE Trans. Geosci. Remote Sens.* **38**, 1387–1398 (2000).

59. D. J. Cavalieri, S. Martin, The contribution of Alaskan, Siberian, and Canadian coastal polynyas to the cold halocline layer of the Arctic Ocean. *J. Geophys. Res.* **99**, 18343–18362 (1994).

60. S. Aoki, K. Ono, D. Hirano, T. Tamura, Continuous winter oceanic profiling in the Cape Darnley Polynya, East Antarctica. *J. Oceanogr.* **76**, 365–372 (2020).